APPLIED SCIENCES AND ENGINEERING

Perovskite nanocomposites as effective CO_2-splitting agents in a cyclic redox scheme

Junshe Zhang,* Vasudev Haribal, Fanxing Li†

We report iron-containing mixed-oxide nanocomposites as highly effective redox materials for thermochemical CO_2 splitting and methane partial oxidation in a cyclic redox scheme, where methane was introduced as an oxygen "sink" to promote the reduction of the redox materials followed by reoxidation through CO_2 splitting. Up to 96% syngas selectivity in the methane partial oxidation step and close to complete conversion of CO_2 to CO in the CO_2-splitting step were achieved at 900° to 980°C with good redox stability. The productivity and production rate of CO in the CO_2-splitting step were about seven times higher than those in state-of-the-art solar-thermal CO_2-splitting processes, which are carried out at significantly higher temperatures. The proposed approach can potentially be applied for acetic acid synthesis with up to 84% reduction in CO_2 emission when compared to state-of-the-art processes.

INTRODUCTION

As a clean and carbon-neutral energy source, solar energy has drawn increasing attention in recent years. To date, solar energy utilization has largely revolved around photovoltaic power generation (*1*–*7*). Although significant progress has been made in photovoltaics, electricity alone only accounts for less than 20% of the global delivered energy consumptions, and the remaining energy is provided by solid, liquid, or gaseous fuels (*8*). Therefore, novel approaches that convert solar energy into fuels offer significant opportunities to reduce fossil fuel consumption in industrial and transportation sectors, thereby providing potentially effective means to mitigate anthropogenic CO_2 emissions.

Solar fuels can be produced from water and CO_2 by photocatalytic splitting under mild conditions (*9*–*14*). However, the efficiency and yields of existing photocatalytic processes are far from satisfactory due to the high thermodynamic and activation barriers of these reactions and challenges in band structure optimization for photocatalysts, electron-hole recombination, and photocatalyst stability (*13*). In addition, product separation for these processes can be problematic (*14*). As an alternative to photocatalytic processes, solar-thermal water/CO_2 splitting has shown excellent potential (*15*–*21*). For instance, solar-to-hydrogen efficiency can be as high as 18% for solar-thermal water splitting, whereas state-of-the-art photocatalytic processes have an energy conversion efficiency of less than 0.2% (*22*). Typical solar-thermal water/CO_2-splitting processes convert concentrated solar energy in a two-step, cyclic redox scheme: A redox material (usually a metal oxide) is first decomposed (or reduced) under an inert environment to (partially) release its lattice oxygen ($MO_x \rightarrow MO_{x-\delta} + \delta/2O_2$) at elevated temperatures (>1200°C), and then the reduced metal oxide is reoxidized (or regenerated) by putting it in contact with water or CO_2 to replenish its lattice oxygen, producing hydrogen or carbon monoxide ($MO_{x-\delta} + \delta H_2O/CO_2 \rightarrow MO_x + \delta H_2/CO$). The resulting hydrogen (H_2) and/or carbon monoxide (CO) can be used as gaseous fuels or converted into liquid fuels or chemicals (*23*, *24*). Such a two-step redox scheme eliminates the need for gas separation and has demonstrated notably higher CO/H_2 production rates (1.35 $mmol_{CO}$ kg_{oxide}^{-1} s^{-1} and 0.71 $mmol_{H2}$ kg_{oxide}^{-1} s^{-1}) when compared to state-of-the-art photocatalytic approaches [~0.07 $mmol_{CO}$ kg_{cat}^{-1} s^{-1} (*21*, *25*)]. The challenge for solar-thermal processes resides in the high reaction temperatures for metal oxide decomposition. Reasonable decomposition rates are only achieved at temperatures above 1500°C for nonvolatile monometallic metal oxides (*15*, *21*, *26*, *27*). Although recent studies on mixed metal oxides have led to notable decreases in the decomposition temperatures, most solar-thermal redox processes require an operating temperature above 1200°C (*17*, *26*–*30*). In addition to the high reaction temperatures, water or CO_2 conversions in these schemes are far from satisfactory (typical below 10%), posing significant challenges for process heat integration and downstream product separations (*31*).

Introducing reducing agents can lower the decomposition (or reduction) temperature (*32*). In such an open-loop thermochemical approach, reducing agents such as carbonaceous fuels are used as oxygen "sinks" to facilitate lattice oxygen extraction from redox materials (*15*). Although significantly lower reduction temperatures (<800°C) have been demonstrated, steam or CO_2 conversion in the subsequent water- or CO_2-splitting step is still very low (*33*–*35*). To address this challenge, we proposed a hybrid solar-redox scheme for water splitting, wherein concentrated solar energy is used to drive the reduction reaction in the presence of methane (CH_4) that undergoes partial oxidation (POx) to produce Fischer-Tropsch (F-T) ready syngas. Using perovskite-supported Fe_3O_4 as the redox material, up to 77% steam-to-hydrogen conversion was achieved (*16*, *36*). Although such a methane-assisted solar-thermal water-splitting scheme is applicable for CO_2 splitting, further increases in water/CO_2-splitting conversion is desirable from process efficiency and product separation standpoints. Another challenge is that iron oxide–based materials tend to overoxidize syngas products in the methane POx step, limiting the syngas selectivity to less than 70%. Herein, we report high-performance redox materials for CO_2 splitting using the aforementioned hybrid solar-redox concept. Perovskite nanocomposites (NCs) exhibit exceptional efficacy for both CO_2 splitting and methane POx: Over 98% CO_2-to-CO conversion was achieved in CO_2 splitting, and syngas selectivity reached 96% in methane POx. As a stand-alone process, methane-assisted CO_2 splitting offers an effective approach for both CO_2 utilization and F-T/methanol ready syngas production. As an example, the resulted syngas and CO products can be readily used for green acetic acid production (Fig. 1). Compared to conventional acetic acid synthesis, the proposed scheme has the potential to reduce fossil fuel consumption by 67% and produce 84% less CO_2 when compared to coal-based process.

Department of Chemical and Biomolecular Engineering, North Carolina State University, Raleigh, NC 27695–7905, USA.
*Present address: School of Chemical Engineering and Technology, Xi'an Jiaotong University, Xi'an, Shaanxi 710049, China.
†Corresponding author. Email: fli5@ncsu.edu

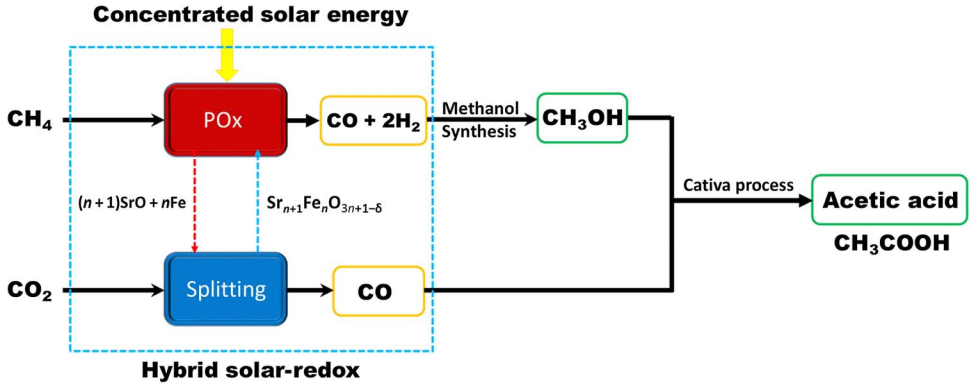

Fig. 1. Hybrid solar-redox process and its application for green acetic acid production from methane and CO_2. This process has three sections: hybrid solar-redox for syngas and CO coproduction, methanol synthesis from the syngas, and acetic acid production.

RESULTS

Rationale for redox material selection

Performance of the redox material is critical to the hybrid solar-redox scheme. Desirable properties for the redox materials include high syngas yield and productivity, excellent CO_2 conversion and CO productivity, and good redox stability. Ideal redox materials should also be affordable, environmentally benign, and attrition-resistant. Among the various metal oxides investigated to date, iron oxide–containing materials are the most promising ones because of their low cost, abundance, and low toxicity (*16*, *17*, *30*–*36*). However, pure iron oxides are not suitable for the proposed redox reactions from a thermodynamics viewpoint.

A methane-assisted thermochemical CO_2-splitting scheme can be described by the reactions listed in Table 1. From a thermodynamic standpoint, the redox material can be considered as an oxygen "source" in the methane POx step and an oxygen sink in the CO_2-splitting step. Hence, a redox pair (MeO_x/MeO_{x-1}) with a high equilibrium oxygen pressure (P_{O2}) can lead to overoxidation of syngas (Eqs. 3 and 4) and low CO_2 conversion (Eq. 7). In contrast, redox pairs with a low P_{O2} will result in low methane conversion (Eq. 2). CO_2 splitting, on the other hand, is monotonically favored at lower P_{O2}. The relationship among equilibrium P_{O2}, syngas yield, and CO_2 conversion, derived from minimizing Gibbs free energy of the reaction set (Eqs. 2 to 6), is illustrated in Fig. 2. As can be seen, equilibrium P_{O2} of Fe/FeO redox pair, which is a commonly used redox material, is away from the ideal (high performance) region for the hybrid solar-redox scheme. This is confirmed by a number of studies that reported low syngas selectivity and limited CO_2 conversions (*16*, *34*–*38*). Thermodynamic analysis suggests that no first-row transition metal oxide has redox properties located in this region (*39*). Unlike monometallic oxides whose redox properties are fixed, mixed metal oxides offer potentially tunable thermodynamic properties. Using iron oxide (FeO) as an example, it can form mixed oxides with strontium oxide (SrO) at various Sr/Fe atomic ratios (*40*). Although SrO is not reducible, formation of Sr-Fe mixed oxides changes the coordination environments and electron density of oxygen anions (O^{2-}). Thus, equilibrium P_{O2} of Sr-Fe mixed oxides can be tailored by adjusting Sr/Fe ratios (Fig. 2). For example, spinel-type $SrFe_2O_4$ exhibits lower P_{O2} than FeO. Further increases in Sr/Fe ratios leads to the formation of perovskite oxides such as Brownmillerite-type $Sr_2Fe_2O_5$ and Ruddlesden-Popper (R-P)–phase $Sr_3Fe_2O_6$ ($Sr_{n+1}Fe_nO_{3n+1-\delta}$ with $n = 2$), both having notably lower P_{O2} than FeO (Fig. 2). Among the three Sr-Fe mixed oxides investigated, $SrFe_2O_4$, with a marginally improved redox performance over FeO, is not an excellent redox material because of low equilibrium syngas yields (<90%) and CO_2 conversions (<95%) at the temperature range of interest. To compare, both $Sr_2Fe_2O_5$ and $Sr_3Fe_2O_6$ can be effective for methane POx and CO_2 splitting, with $Sr_3Fe_2O_6$ offering improved redox properties for the hybrid solar-redox scheme.

Table 1. Main reactions that occur in methane POx and CO_2 splitting in the redox scheme.

Methane POx		CO_2 splitting	
$MeO_x \leftrightarrows MeO_{x-1} + {}^1/_2O_2$	(1)	$CO_2 \leftrightarrows CO + {}^1/_2O_2$	(7)
$CH_4 + {}^1/_2O_2 \leftrightarrows CO + 2H_2$	(2)	$MeO_{x-1} + {}^1/_2O_2 \leftrightarrows MeO_x$	(8)
$CO + {}^1/_2O_2 \leftrightarrows CO_2$	(3)		
$2H_2 + O_2 \leftrightarrows H_2O$	(4)		
$2CO \leftrightarrows C + CO_2$	(5)		
$CO + H_2O \leftrightarrows H_2 + CO_2$	(6)		

Redox performance of $Sr_3Fe_2O_{7-\delta}$

As-prepared $Sr_3Fe_2O_{7-\delta}$ (SF_7) exhibits excellent redox activity (figs. S1 and S2), but it deactivates continuously (fig. S3) at 900°C under a weight hourly space velocity (WHSV) of 60,000 $cm^3\ g_{SF7}^{-1}\ hour^{-1}$. Specifically, syngas productivity (eq. S1) dropped by 82% in the methane POx step, and CO productivity (eq. S2) decreased by 72% in the CO_2-splitting step over 15 redox cycles. It is noted that even with significant deactivation, CO productivity in the 16th cycle (2.6 mol kg_{SF7}^{-1}) is still an order of magnitude higher than that in state-of-the-art solar-thermal CO_2-splitting schemes [<0.3 mol kg_{oxide}^{-1} for ceria and perovskites (*21*, *29*, *41*, *42*)]. $Sr_3Fe_2O_{7-\delta}$ is also superior to CeO_2-modified Fe_2O_3 in a H_2-assisted thermochemical CO_2-splitting scheme, where CO productivity is about 1.1 mol kg_{oxide}^{-1} (*35*). To shed light on the cause of deactivation, we acquired energy-dispersive x-ray spectroscopy (EDS) mapping and x-ray diffraction (XRD) patterns of as-prepared and spent samples (fig. S4). XRD measurements and thermogravimetric analysis suggest that the as-prepared sample has an R-P–phase $Sr_3Fe_2O_{6.75}$ (tetragonal *I*4/*mmm*), whose oxygen stoichiometry decreases to about 6 in an inert atmosphere at 900°C. Metallic iron, iron carbides, Fe_3O_4, and SrO were detected after the first reduction. It was found that CO_2 can fully reoxidize metallic iron back to the R-P phase, but a significant portion of $Sr_3Fe_2O_6$ becomes unreducible in the 16th reduction (fig. S4). Elemental mappings indicate that significant phase segregation

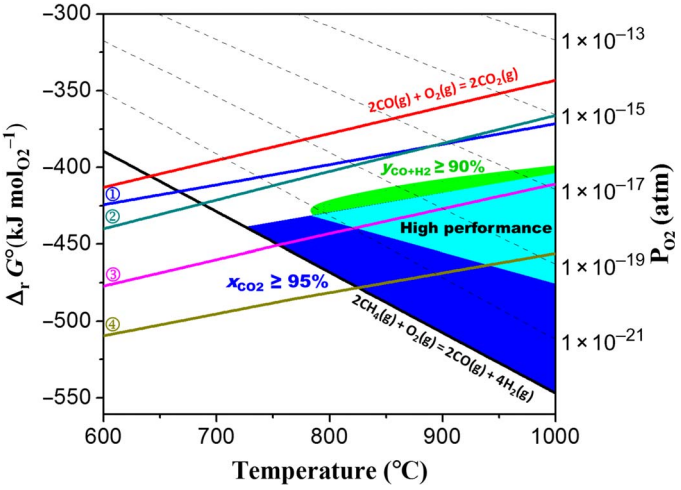

Fig. 2. Thermodynamic analysis of methane POx/CO_2-splitting reactions and selected redox materials. Standard Gibbs free energy change ($\Delta_r G°$) of the oxidation reactions (①2Fe + O_2 = 2FeO; ②$^2/_3$SrO + $^4/_3$Fe + O_2 = $^2/_3$SrFe$_2$O$_4$; ③$^4/_3$SrO + $^4/_3$Fe + O_2 = $^2/_3$Sr$_2$Fe$_2$O$_5$; and ④2SrO + $^4/_3$Fe + O_2 = $^2/_3$Sr$_3$Fe$_2$O$_6$) and corresponding equilibrium oxygen partial pressures (P_{O2}), for ≥95% CO_2 conversions (blue region) and ≥90% methane-to-syngas yield (green region) at 1 atm. The overlapping (cyan) zone is the ideal (high performance) region for both methane POx and CO_2-splitting reactions.

and sintering occurred in redox reactions (fig. S4); this may have caused the redox activity to decrease. To retard sintering and deactivation, the redox active-phase (SF_7) was dispersed in an inert and earth-abundant calcium manganese oxide ($Ca_{0.5}Mn_{0.5}O$) phase.

$Sr_3Fe_2O_{7-\delta}$-$Ca_{0.5}Mn_{0.5}O$ NCs

Formation of $Sr_3Fe_2O_{7-\delta}$-$Ca_{0.5}Mn_{0.5}O$ NCs (SF_7-CM NCs) is revealed by electron microscopy (figs. S5 and S6), and reducibility of the sample is characterized by hydrogen temperature-programmed reduction (H_2-TPR) and in situ XRD (figs. S7 and S8). The redox stability of SF_7-CM NCs is shown in Fig. 3. Both syngas productivity in the methane POx step and CO productivity in the CO_2-splitting step decreased slightly in the first 21 cycles and then stabilized in the subsequent 9 cycles at 900°C at a WHSV of 24,000 cm^3 $g_{SF7\text{-}CM}^{-1}$ hour^{-1}. Specifically, syngas productivity decreased from 4.42 to 4.28 mol $kg_{SF7\text{-}CM}^{-1}$, whereas CO productivity varied from 1.74 to 1.53 mol $kg_{SF7\text{-}CM}^{-1}$ over the first 21 cycles. In the CO_2-splitting step, CO productivity was significantly higher for SF_7-CM NCs than for CeO_2-Fe_2O_3 [1.1 mol kg_{oxide}^{-1} (*35*)]. In the last 10 cycles, syngas selectivity was higher than 95% in the methane POx step. Moreover, the molar ratio of H_2/CO remained around 1.96, and coke formation was negligible between 20 and 30 cycles. The excellent stability of the NCs is attributed to the confinement effect that involves dispersing an active phase in an inert medium. XRD measurements demonstrated that $Ca_{0.5}Mn_{0.5}O$ acted as a dispersing medium (Fig. 3), which itself had no activity toward the redox reactions. In addition, elemental mappings demonstrate that all elements are uniformly distributed in as-prepared and spent samples (figs. S9 and S10).

Figure 4A shows typical gaseous product elution profiles in the methane POx step of the 30th cycle. After feeding CH_4 to the NC bed, CO_2 coeluted with CO and H_2, but its elution profile was different from those of CO and H_2. The peak production rates for CO_2, CO, and H_2 were 0.51, 4.14, and 8.03 mmol $kg_{SF7\text{-}CM}^{-1}$ s^{-1} at 16, 250, and 250 s, respectively. Such a pattern is typical for the redox-based methane POx (*43*). The gaseous compound elution profiles in the CO_2-splitting

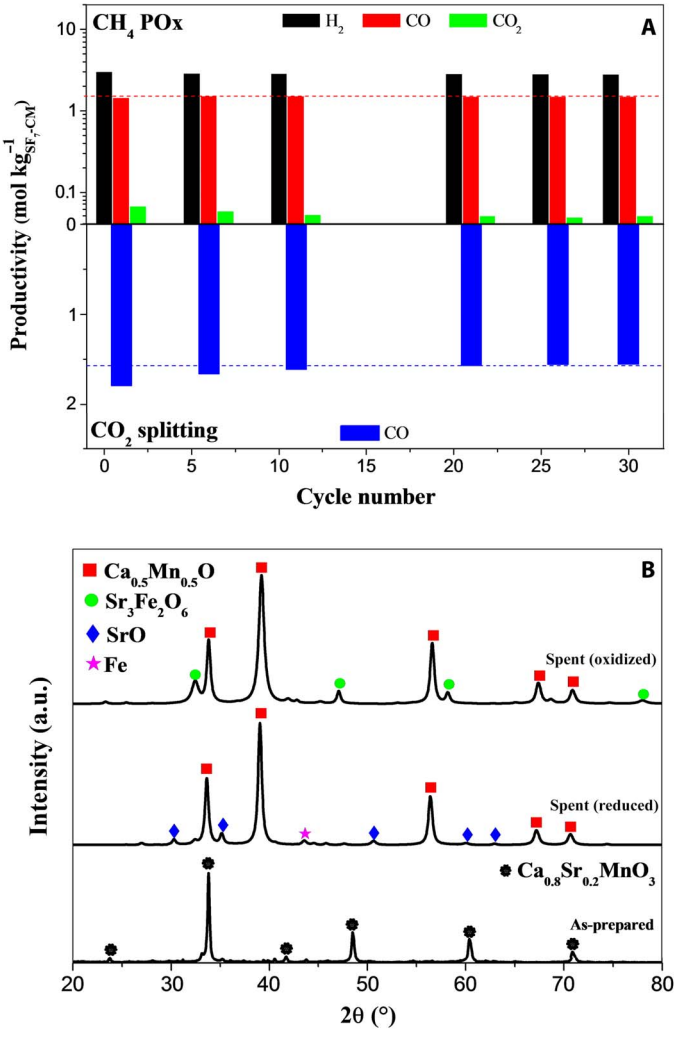

Fig. 3. Redox stability of SF_7-CM NCs. (**A**) Productivity of H_2, CO, and CO_2 in methane POx and CO in CO_2 splitting. (**B**) XRD patterns of spent samples. Reaction conditions: $m_{SF7\text{-}CM}$ = 0.25 g; T = 900°C, F = 74.4 μmol s^{-1}, P = 1 atm, y_{CH4} = 0.1, and y_{CO2} = 0.1. a.u., arbitrary units.

step of the 30th cycle are presented in Fig. 4B. The breakthrough time of CO_2, which is the time when CO_2 flow rate at the outlet of a reactor reaches 2% of that at the inlet, was 35 s, and it coincided with the time at which the CO production rate maximized (22 $mmol_{CO}$ $kg_{SF7\text{-}CM}^{-1}$ s^{-1}). The peak CO production rate in this open-loop thermochemical scheme was one order of magnitude higher than that in conventional solar-thermal CO_2 splitting, which was carried out at temperatures 200°C higher than that in the former (*21*). It should be noted that the breakthrough curve of CO_2 depends on factors like the flow rate of feed, amount of redox materials, and inlet concentration of CO_2. As shown in Fig. 4B, CO_2 flow rate leveled off after 180 s. In the first 3 min, the average CO production rate was 8.23 mmol $kg_{SF7\text{-}CM}^{-1}$ s^{-1}, significantly higher than that (<3 mmol kg_{oxide}^{-1} s^{-1}) in a recently reported methane-assisted thermochemical scheme (*33*).

One key issue with thermochemical CO_2-splitting studies conducted to date is the incomplete CO_2 conversion (<90%). For SF_7-CM NCs, near-complete CO_2 conversion was achieved during the early stage of the reaction (fig. S11). However, the average CO_2 conversion in the first 3 min was only 32.3% in the 30th cycle (Fig. 4B). To improve

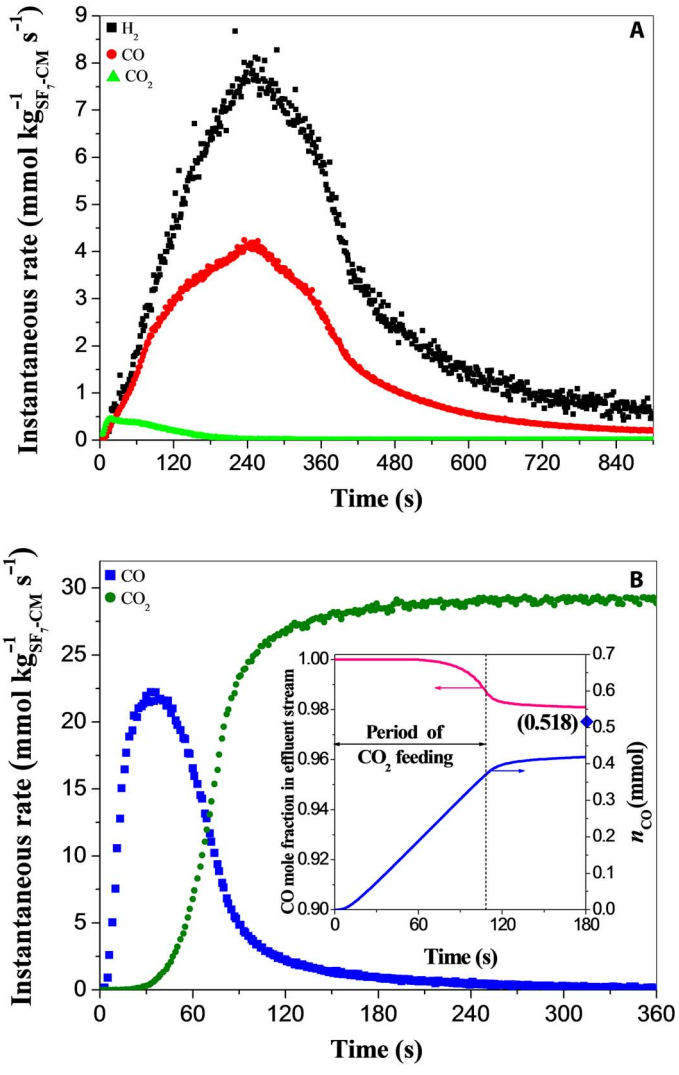

Fig. 4. Instantaneous production rates of gaseous products from the redox reactions using SF_7-CM NCs. (**A**) Elution profiles of H_2, CO, and CO_2 in methane POx at the 30th cycle. (**B**) Elution profiles of CO and CO_2 in CO_2 splitting at the 30th cycle. Inset in (B) is the cumulative CO molar fraction in the product and moles of CO produced in CO_2 splitting for a short feeding period (the blue dot denotes the total moles of CO produced for complete regeneration). Reaction conditions: $m_{SF7\text{-}CM}$ = 0.25 g; T = 900°C, F = 74.4 μmol s^{-1}, P = 1 atm, y_{CH4} = 0.1 (A), and y_{CO2} = 0.1 (main figure) and 0.05 (inset) (B).

CO_2 conversion, we attempted to shorten the duration of the CO_2-splitting step. As shown in Fig. 4B, CO_2 conversion was above 98%, and the average CO production rate was 13.8 mmol $kg_{SF7\text{-}CM}^{-1}$ s^{-1} for a shorter feeding period. Such a short regeneration period was adequate to replenish over 80% of the active lattice oxygen of the reduced NCs. To the best of our knowledge, such a high CO_2 conversion has yet to be reported for thermochemical CO_2 splitting. These findings clearly demonstrate that this NC outperforms the other redox materials for thermochemical CO_2 splitting.

$SrFeO_{3-\delta}$-CaO NCs

To further verify the role of the dispersing medium, we prepared another NC with $SrFeO_{3-\delta}$ as the active phase and CaO dispersing medium. $SrFeO_3$ has the highest oxygen capacity among the R-P–type perovskite family ($Sr_{n+1}Fe_nO_{3n+1}$, $n = \infty$) while still having desirable redox properties (Fig. 2). XRD and Rietveld refinement do not indicate significant Ca substitution of Sr in $SrFeO_{3-\delta}$ phase in the NCs, and excess Sr atoms were incorporated into the crystal structure of CaO (figs. S12 and S13). Redox testing indicated that the CaO phase significantly enhanced the redox kinetics, leading to more than 10-fold faster methane POx and CO_2 splitting (figs. S14 and S15). Apart from the faster redox kinetics, the redox stability of $SrFeO_{3-\delta}$-CaO NCs (SF_3-C NCs) was also excellent at 900°C. After the first two cycles, syngas (H_2/CO ≅ 2) productivity and selectivity (eq. S3) maintained at around 5.8 mol $kg_{SF3\text{-}C}^{-1}$ and 96%, respectively, in the methane POx step (fig. S16). Meanwhile, CO productivity in the CO_2-splitting step decreased slightly over the first 10 cycles (less than 9%) and then remained unchanged between 10 and 16 cycles (fig. S16). The stability was further confirmed by XRD analysis, which demonstrated that the 1st and 16th reduced samples exhibited identical XRD patterns with iron reduced to its metallic form (fig. S17).

As demonstrated earlier, it is possible to achieve high CO_2 conversion by partially replenishing the active lattice oxygen. Meanwhile, high methane conversion can be reached with partially reoxidized NCs (for example, 90% reoxidation). For these POx/splitting cycles, both methane and CO_2 conversions were high compared to complete reduction/oxidation cycles but with slightly lowered syngas and CO productivity. The redox stability of SF_3-C NCs that underwent partial reduction and oxidation at 980°C with a WHSV of 12,000 cm^3 $g_{SF3\text{-}C}^{-1}$ $hour^{-1}$ is shown in Fig. 5. In the methane POx step, syngas (H_2/CO ≅ 2.13) productivity maintained at around 4.63 mol $kg_{SF3\text{-}C}^{-1}$ after 13 cycles with insignificant CO_2 production (<0.08 mol $kg_{SF3\text{-}C}^{-1}$). After the redox material stabilized, methane conversion reached 59%, and syngas selectivity was around 90% (fig. S18 and table S1). In the CO_2-splitting step, CO_2 conversion was 98%, the average CO production rate was 9.13 mmol $kg_{SF3\text{-}C}^{-1}$ s^{-1}, and CO productivity was 2.17 mol $kg_{SF3\text{-}C}^{-1}$ in the last 17 cycles. A further increase in syngas yield can be realized by tuning the redox window of SF_3-C NCs. Over partially reoxidized SF_3-C NCs, methane conversion of 90% was achieved with 89% syngas selectivity (table S2) at 980°C with a WHSV of 2045 cm^3 $g_{SF3\text{-}C}^{-1}$ $hour^{-1}$. Moreover, CO_2 conversion was nearly 100% in the CO_2-splitting step before methane POx (fig. S19).

DISCUSSION

The hybrid solar-redox scheme offers various attractive options for CO_2 utilization and liquid fuel/chemical production. Here, acetic acid production was investigated as an example. Direct conversion of methane and CO_2 to acetic acid is thermodynamically unfavorable, albeit being atom-economic (*44*). State-of-the-art approach is the syngas route: Coal is first gasified to produce syngas, and then the syngas is cleaned and conditioned to remove excess CO and CO_2. This is followed by methanol synthesis ($CO + 2H_2 \leftrightarrows CH_3OH$) and subsequent carbonylation of methanol ($CH_3CHO + CO \leftrightarrows CH_3COOH$). Methane is not an ideal feedstock for acetic acid synthesis via the conventional syngas route because the CO/H_2 ratio is too low in methane-derived syngas. The solar-driven redox process, as shown in Fig. 1 , produces a pure CO stream and a syngas stream with ideal compositions for methanol synthesis. Thus, the need for costly separation processes is eliminated.

The solar-driven redox process has three main sections (Fig. 1 and fig. S20): (i) the hybrid solar-redox section where syngas and CO are produced, (ii) the methanol synthesis section that converts syngas into methanol (*45*), and (iii) the acetic acid synthesis section in which methanol

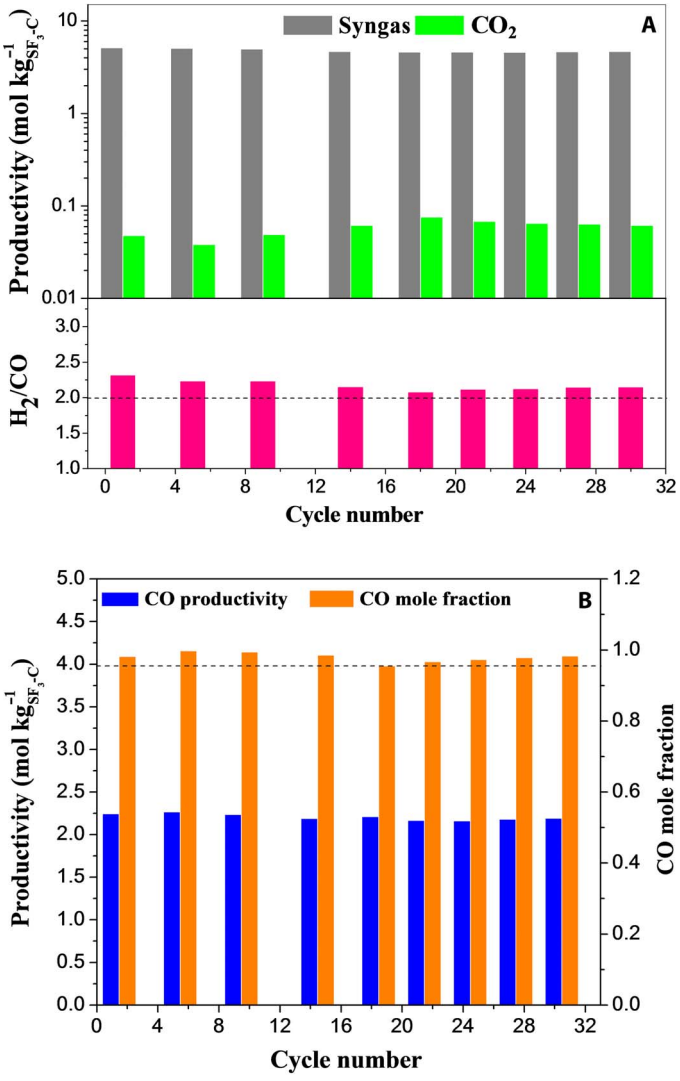

Fig. 5. Redox stability of SF_3-C NCs. (**A**) Productivity of syngas and CO_2 and H_2/CO molar ratio in the methane POx step. (**B**) Productivity of CO and CO molar fraction in the product during the CO_2-splitting step; the dashed line denotes the CO mole fraction of 0.95. In all 30 redox cycles, methane conversion is greater than 58%, and CO_2 conversion is above 94%. Reaction conditions: $m_{SF3\text{-}C}$ = 0.25 g; T = 980°C, F = 37.2 μmol s^{-1}, P = 1 atm, y_{CH4} = 0.1, and y_{CO2} = 0.1.

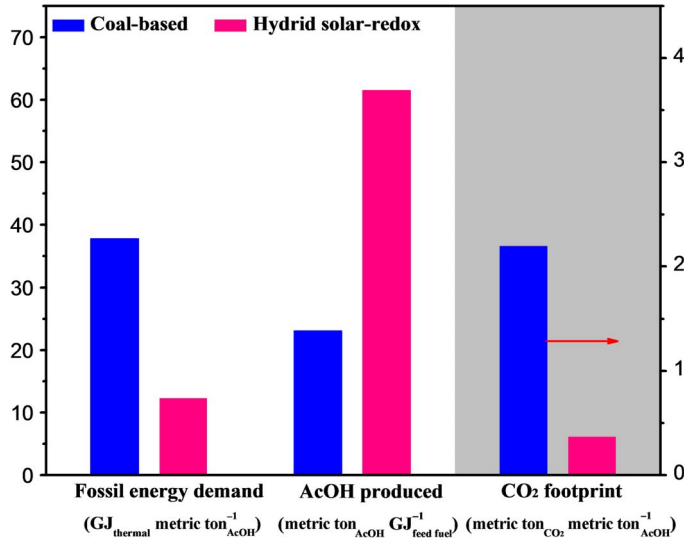

Fig. 6. Comparison of the conventional and hybrid solar-redox processes for acetic acid production. The hybrid solar-redox process (see Fig. 1) is compared with the traditional coal-based process to obtain syngas. For the coal-based process, all energy demand is provided by coal. For the hybrid solar-redox process, the total energy demand is 20.4 $GJ_{thermal}$ per metric ton of acetic acid (AcOH), and 39.2% (8 $GJ_{thermal}$ metric ton_{AcOH}^{-1}) is provided by solar energy.

and CO are converted to acetic acid by the Cativa process (*46*). Using ASPEN Plus, the overall energy required for the process was calculated. This process was compared with a coal-based scheme (fig. S21) (*47*). For each metric ton of acetic acid produced, 20.4 $GJ_{thermal}$ is required in the solar-driven process, whereas 37.8 $GJ_{thermal}$ is needed in the coal-based process (Fig. 6). Regarding the productivity, the former produces 2.7 times as much acetic acid as the latter per gigajoule of feed fuel (Fig. 6). Simulation results suggest that production of 1 metric ton of acetic acid results in 0.37 metric ton of CO_2 in the solar-driven process but 2.2 metric tons CO_2 in the coal-based approach.

We report iron-containing mixed metal oxides as effective CO_2-splitting and methane POx agents in a cyclic redox scheme. Unsupported $Sr_3Fe_2O_{7-\delta}$ demonstrated extraordinary methane POx and CO_2-splitting activity at 900°C. However, it deactivated over redox cycles. Dispersing $Sr_3Fe_2O_{7-\delta}$ in a $Ca_{0.5}Mn_{0.5}O$ matrix significantly enhanced the redox stability of the R-P–structured $Sr_3Fe_2O_{7-\delta}$. Further investigation of the perovskite-structured $SrFeO_{3-\delta}$ compositing with CaO indicated that the inert CaO phase not only enhanced the redox kinetics but also improved its redox stability at 900° to 980°C. At 980°C, the redox activity decreased slightly in the first 13 cycles and then remained unchanged in the last 17 cycles. In the last 17 cycles, the average CO production rate was 9.13 mmol $kg_{SF\text{-}C}^{-1}$ s^{-1}, and CO productivity was 2.17 mol $kg_{SF3\text{-}C}^{-1}$. The former is 6.8 times higher than state-of-the-art solar-thermal CO_2-splitting schemes (1.35 mmol kg_{oxide}^{-1} s^{-1}) carried out at significantly higher temperatures (above 1200°C), and the latter is sevenfold higher than that in solar-thermal schemes (<0.3 mol kg_{oxide}^{-1}). For partially reoxidized SF_3-C NCs, methane conversion reached 90% with 89% syngas selectivity at 980°C with a WHSV of 2045 cm^3 $g_{SF3\text{-}C}^{-1}$ $hour^{-1}$. Moreover, CO_2-to-CO conversion maintained at near 100% in the CO_2-splitting step. The exceptionally high CO_2 utilization efficiency and high syngas yield make the redox materials and the hybrid solar-redox scheme potentially attractive. Process simulations indicate that the fossil energy consumption for acetic acid production can be reduced by 67% by the hybrid solar-redox process when compared to the state-of-the-art one while reducing CO_2 emission by as much as 84%.

MATERIALS AND METHODS

Synthesis of the redox materials

For the synthesis of SF_7-CM NCs [18 weight % (wt %) SF_7], 0.83 g of strontium nitrate [$Sr(NO_3)_2$], 3.71 g of calcium nitrate [$Ca(NO_3)_2{\cdot}4H_2O$], 4.94 g of manganese nitrate [$Mn(NO_3)_2{\cdot}4H_2O$], and 18.90 g of citric acid ($C_6H_8O_7$) were dissolved in 80 ml of deionized (DI) water. The solution was then heated up to 40°C under agitation (600 rpm) on a hot plate, followed by maintaining at this temperature for 30 min. After that, 9.18 g of ethylene glycol ($C_2H_6O_2$) was added to the above solution. The resulted solution was subsequently heated up to 80°C and then kept at this temperature until a polymeric gel (ca. 25 cm^3) was formed. Iron oxide dispersion was prepared by ultrasonicating

0.50 g of nanoparticles in 51.5 g of 22.3 to 77.7 wt % ethylene glycol/water solution. The dispersion was then transferred to a 50-ml centrifuge tube, followed by centrifuging at 3500 rpm for 5 min. Around 30 ml of the upper part of the nanoparticle suspension was mixed with 20 ml of gel. The mixture was ultrasonicated for 15 min and then heated up to 80°C, followed by holding at this temperature for 2 days. Afterward, the gel was dried at 120°C overnight to evaporate the residual water. The dry precursor was put in a high-purity alumina crucible, which was then placed in a high-purity alumina ceramic tube that was mounted on an MTI furnace (GSL-1500X-50-UL), into which air continuously flew. The tube was heated up from room temperature to 1200°C for 300 min and then held at this temperature for 12 hours, followed by cooling down to 300°C for 300 min.

For the synthesis of SF_3-C NCs (26 wt % $SrFeO_{3-\delta}$), 0.70 g of $Sr(NO_3)_2$, 0.90 g of iron nitrate [$Fe(NO_3)_2{\cdot}9H_2O$], 4.57 g of $Ca(NO_3)_2{\cdot}4H_2O$, and 11.97 g of $C_6H_8O_7$ were dissolved into 80 ml of DI water. The solution was then heated up to 40°C under agitation (600 rpm), followed by maintaining at this temperature for 30 min. After that, 5.80 g of $C_2H_6O_2$ was added. The resulted solution was further heated up to 80°C and then kept at this temperature until a polymer gel formed. Afterward, the gel was dried at 120°C overnight to evaporate the residual water. Finally, the dry precursor was calcined at 1200°C in air for 12 hours, as described before.

For the synthesis of $Sr_3Fe_2O_{7-\delta}$ and $SrFeO_{3-\delta}$, these two redox materials were prepared by the Pechini method as described above. The molar ratio of Sr/Fe in the precursor solutions was 3:2 and 1:1 for $Sr_3Fe_2O_{7-\delta}$ and $SrFeO_{3-\delta}$, respectively. The molar ratio of $C_2H_6O_2$/$C_6H_8O_7$/total cations was 3.75:2.5:1 in the gel. The calcination temperature was 1200°C.

Material characterization

The oxygen stoichiometry of as-prepared redox materials was determined by H_2-TPR, which was carried out on a TA Instruments thermogravimetric analyzer (SDT Q600). About 50 mg of the sample was loaded into an alumina crucible. Before measurements, the as-prepared sample was treated at 900°C for 1 hour in 20 volume percent (volume %) O_2/80 volume % Ar (74.4 μmol s^{-1}). After treatment, the sample was cooled down and subsequently heated up to 100°C and then kept at this temperature for 30 min in 10 volume % H_2/90 volume % Ar (74.4 μmol s^{-1}). Then, it was heated up to 1150°C at a ramping rate of 10°C min^{-1}. To obtain O_2- or CO_2-regenerated sample, the sample was first reduced in 10% CH_4/90% Ar (74.4 μmol s^{-1}) and then oxidized in 10% O_2 (or CO_2)/90% Ar (74.4 μmol s^{-1}) at 900°C, followed by cooling down to room temperature. The oxygen stoichiometry of redox materials under inert conditions was estimated from the amount of lattice oxygen released from the as-prepared sample (after 20% O_2 pretreatment) at a temperature range of ~25° to 900°C in Ar. Around 580 mg of the sample was loaded to a U-type quartz tube ($Ø_{in}$ = 4 mm), and quartz wool was packed on both ends of the oxide bed to keep the particles in place. The reactor was heated up to 900°C in Ar (22.32 μmol s^{-1}). The effluent stream was monitored by an MKS Cirrus 2 quadrupole mass spectrometer (QMS).

Rietveld analysis of the sample's XRD patterns at room temperature before and after treating at 900°C in nitrogen was also performed. The XRD patterns were acquired on an Empyrean PANalytical XRD using a Cu Kα radiation (λ = 0.1542 nm) operating at 45 kV and 40 mA, which was equipped with an XRK 900 reactor chamber. A sample pellet was placed on a glass ceramics holder (Ø = 15 mm) in the high-temperature chamber, and the sample was scanned at a 2θ range of 20° to 110° with a step size of 0.012°. The sample was heated up from 25° to 900°C in 30 min and then held at this temperature for 1.5 hours in nitrogen. Finally, the sample was cooled down to room temperature in nitrogen. Powder XRD measurements of as-prepared and spent samples under ambient conditions were performed on a Bragg-Brentano x-ray diffractometer (Rigaku SmartLab) at a 2θ range of 20° to 80° with a step size of 0.05°, using graphite monochromatic Cu Kα radiation (λ = 0.1542 nm) with a nickel filter and operating at 40 kV and 44 mA.

To examine the phase properties during the reduction of SF_7-CM NC, we performed in situ crystallographic analyses of the sample on an Empyrean PANalytical XRD using a Cu Kα radiation operating at 45 kV and 40 mA, which is equipped with a disk-shaped high-temperature chamber. A sample pellet was placed on an alumina sample holder (Ø = 15 mm) in the high-temperature chamber, and the sample was scanned at a 2θ range of 20° to 80° with a step size of 0.1° and a scanning time of 0.1 s at each step. The sample was heated up from 25° to 675°C at an interval of 50°C in 5% H_2/95% He with a ramping rate of 5°C min^{-1}. At each step, the temperature was held for 5 min.

High-resolution transmission electron microscope (TEM) images were obtained with a field-emission scanning transmission electron microscope (STEM) (JEOL 2010 F) operating at 200 kV. STEM images and mapping were obtained on an aberration-corrected (S)TEM (FEI Titan 80-300) operating at 200 kV. The sample was prepared by drop-casting a suspension of sample in ethanol (200 proof, anhydrous) on a carbon-coated copper grid and then drying it under ambient conditions. Scanning electron microscope (SEM) images were obtained on a Verios 400 (FEI) field-emission microscope and a JSM-6010LA.

To determine the bulk composition of NC, samples were digested with hot concentrated nitric acid. The aliquots were filtered with a 0.45-μm filter (Whatman), and the metal concentrations were analyzed by using an inductively coupled plasma (ICP) optical emission spectrometry (PerkinElmer ICP Optical Emission Spectrometer model 8000).

N_2 physisorption was performed at −196°C on a volumetric adsorption analyzer (Micromeritics ASAP 2020). Before the analysis, the sample was outgassed under vacuum at 300°C for 2 hours. The specific surface area was calculated by using the Brunauer-Emmett-Teller method in the relative pressure range from 3×10^{-6} to 0.2.

Reactor setup and redox experiments

The redox performance was evaluated in a microreactor (U-type quartz tube; $Ø_{in}$ = 4 mm) that was vertically placed inside an electric furnace. The furnace was equipped with a K-type thermocouple whose tip touched the outside of the quartz tube at the location of the redox material. The gas flows were controlled by MCQ mass flow controllers (Alicat). The composition of the effluent stream was monitored by QMS.

In a typical experiment, 0.25 g of the redox material (250 to 425 μm) was loaded into the reactor, and quartz wool was packed on both ends of the oxide bed to keep the particles in place. The reactor was heated up to the targeted temperature in Ar (66.96 μmol s^{-1}), and then these conditions were maintained for around 30 min to remove the residual air in the reaction system. After that, a CH_4 stream (7.44 μmol s^{-1}) was introduced to the Ar stream, and methane POx lasted for 15 min, followed by purging the reactor with Ar (66.96 mmol s^{-1}) for 10 min. Next, a CO_2 stream (7.44 μmol s^{-1}) was introduced to the Ar stream, and CO_2 splitting lasted for 10 min, followed by purging the reactor with Ar (66.96 μmol s^{-1}) for 10 min. The above POx-splitting cycle was repeated 30 times. In the redox test with SF_3-C NCs at 980°C, the amount of coke formed in the POx step was determined by in situ

oxidizing the NCs in 10% O_2/90% Ar (37.2 μmol s^{-1}) at 900°C while measuring the CO_x production with QMS.

The first reduced sample was recovered after the first methane POx step, and the last oxidized sample was collected after the redox experiment was completed. The last reduced sample was prepared by reducing part of the last oxidized sample in 10 volume % CH_4/90 volume % Ar (74.4 μmol s^{-1}) at 900°C for 15 min.

SUPPLEMENTARY MATERIALS

Supplementary material for this article is available at http://advances.sciencemag.org/cgi/content/full/3/8/e1701184/DC1

Supplementary Text

fig. S1. Characterization of $Sr_3Fe_2O_{7-\delta}$.

fig. S2. Redox kinetics on $Sr_3Fe_2O_{7-\delta}$.

fig. S3. Redox stability of $Sr_3Fe_2O_{7-\delta}$.

fig. S4. Characterization of as-prepared and spent $Sr_3Fe_2O_{7-\delta}$ under ambient conditions.

fig. S5. Characterization of as-prepared and spent (oxidized) SF_7-CM NCs.

fig. S6. STEM image and EDS elemental mapping of as-prepared SF_7-CM NCs.

fig. S7. H_2-TPR of SF_7-CM NCs.

fig. S8. In situ XRD patterns of as-prepared SF_7-CM NCs during reduction in hydrogen atmosphere at a temperature range of 25° to 675°C.

fig. S9. STEM image and EDS elemental mapping of spent (reduced) SF_7-CM NCs after 30 cycles.

fig. S10. STEM image and EDS elemental mapping of spent (oxidized) SF_7-CM NCs after 30 cycles.

fig. S11. CO_2 splitting on SF_7-CM NC after methane POx.

fig. S12. Characterization of $SrFeO_{3-\delta}$.

fig. S13. Characterization of SF_3-C NCs.

fig. S14. Redox kinetics on $SrFeO_{3-\delta}$.

fig. S15. Redox kinetics on SF_3-C NCs.

fig. S16. Redox stability of SF_3-C NCs.

fig. S17. Characterization of as-prepared and spent SF_3-C NCs under ambient conditions.

fig. S18. Redox kinetics over SF_3-C NCs in a short redox period.

fig. S19. Redox kinetics over SF_3-C NCs.

fig. S20. Block diagram for the hybrid solar-redox (HSR)–AcOH.

fig. S21. Block diagram for AcOH synthesis using coal-slurry gasifier (CG).

fig. S22. Comparison in the overall energy demand and production of AcOH for CG and HSR processes.

fig. S23. CO_2 footprint of the two processes.

table S1. Product analysis of the last redox cycle over SF_3-C NCs.

table S2. Product analysis of a short POx over SF_3-C NCs at 980°C.

table S3. Description of the ASPEN Plus model.

table S4. ASPEN Plus modules, property methods, and databanks.

table S5. Comparison of CG and HSR-AcOH.

References (*48*–*52*)

REFERENCES AND NOTES

1. H. Tsai, W. Nie, J.-C. Blancon, C. C. Stoumpos, R. Asadpour, B. Harutyunyan, A. J. Neukirch, R. Verduzco, J. J. Crochet, S. Tretiak, L. Pedesseau, J. Even, M. A. Alam, G. Gupta, J. Lou, P. M. Ajayan, M. J. Bedzyk, M. G. Kanatzidis, A. D. Mohite, High-efficiency two-dimensional Ruddlesden–Popper perovskite solar cells. *Nature* **536**, 312–316 (2016).
2. D. P. McMeekin, G. Sadoughi, W. Rehman, G. E. Eperon, M. Saliba, M. T. Hörantner, A. Haghighirad, N. Sakai, L. Korte, B. Rech, M. B. Johnston, L. M. Herz, H. J. Snaith, A mixed-cation lead mixed-halide perovskite absorber for tandem solar cells. *Science* **351**, 151–155 (2016).
3. N. J. Jeon, J. H. Noh, W. S. Yang, Y. C. Kim, S. Ryu, J. Seo, S. I. Seok, Compositional engineering of perovskite materials for high-performance solar cells. *Nature* **517**, 476–480 (2015).
4. W. Nie, H. Tsai, R. Asadpour, J.-C. Blancon, A. J. Neukirch, G. Gupta, J. J. Crochet, M. Chhowalla, S. Tretiak, M. A. Alam, H.-L. Wang, A. D. Mohite, High-efficiency solution-processed perovskite solar cells with millimeter-scale grains. *Science* **347**, 522–525 (2015).
5. H. Zhou, Q. Chen, G. Li, S. Luo, T.-b. Song, H.-S. Duan, Z. Hong, J. You, Y. Liu, Y. Yang, Interface engineering of highly efficient perovskite solar cells. *Science* **345**, 542–546 (2014).
6. A. Mei, X. Li, L. Liu, Z. Ku, T. Liu, Y. Rong, M. Xu, M. Hu, J. Chen, Y. Yang, M. Grätzel, H. Han, A hole-conductor–free, fully printable mesoscopic perovskite solar cell with high stability. *Science* **345**, 295–298 (2014).
7. J. Jean, P. R. Brown, R. L. Jaffe, T. Buonassisid, V. Bulovic, Pathways for solar photovoltaics. *Energy Environ. Sci.* **8**, 1200–1219 (2015).
8. U.S. Energy Information Administration (EIA), International Energy Outlook 2016 (EIA, 2016); www.eia.gov/outlooks/ieo/pdf/0484(2016).pdf [accessed 29 June 2017].
9. R. Kuriki, H. Mastunaga, T. Nakashima, K. Wada, A. Yamakata, O. Ishitani, K. Maeda, Nature-inspired, highly durable CO_2 reduction system consisting of a binuclear ruthenium(II) complex and an organic semiconductor using visible light. *J. Am. Chem. Soc.* **138**, 5159–5170 (2016).
10. H. Takeda, K. Ohashi, A. Sekine, O. Ishitani, Photocatalytic CO_2 reduction using Cu(I) photosensitizers with a Fe(II) catalyst. *J. Am. Chem. Soc.* **138**, 4354– 4357 (2016).
11. J. Liu, Y. Liu, Y. Hang, X. Zhang, H. Huang, Y. Lifshitz, S.-T. Lee, J. Zhong, A. Kang, Metal-free efficient photocatalyst for stable visible water splitting via a two-electron pathway. *Science* **347**, 970–974 (2015).
12. T. Hisatomi, J. Kubota, K. Domen, Recent advances in semiconductors for photocatalytic and photoelectrochemical water splitting. *Chem. Soc. Rev.* **43**, 7520–7535 (2014).
13. W. Wu, Y. Zhou, Z. Zou, Photocatalytic conversion of CO_2 into renewable hydrocarbon fuels: State-of-the-art accomplishment, challenges, and prospects. *Adv. Mater.* **27**, 4607–4626 (2015).
14. X. Chang, T. Wang, J. Gong, CO_2 photo-reduction: Insights into CO_2 activation and reaction on surfaces of photocatalysts. *Energy Environ. Sci.* **9**, 2177–2196 (2016).
15. C. Agrafiotis, M. Roeb, C. Sattler, A review on solar thermal syngas production via redox pair-based water/carbon dioxide splitting thermochemical cycles. *Renew. Sustain. Energy Rev.* **42**, 254–285 (2015).
16. F. He, J. Trainham, G. Parsons, J. S. Newman, F. Li, A hybrid solar-redox scheme for liquid fuel and hydrogen coproduction. *Energy Environ. Sci.* **7**, 2033–2042 (2014).
17. C. L. Muhich, B. W. Evanko, K. C. Weston, P. Lichty, X. Liang, J. Martinek, C. B. Musgrave, A. W. Weimer, Efficient generation of H_2 by splitting water with an isothermal redox cycle. *Science* **341**, 540–542 (2013).
18. J. Kim, T. A. Johnson, J. E. Miller, E. B. Stechl, C. T. Maravelias, Fuel production from CO_2 using solar-thermal energy: System level analysis. *Energy Environ. Sci.* **5**, 8417–8429 (2012).
19. B. Xu, Y. Bhawe, M. E. Davis, Low-temperature, manganese oxide-based, thermochemical water splitting cycle. *Proc. Natl. Acad. Sci. U.S.A.* **109**, 9260–9264 (2012).
20. J. Kim, C. A. Herron, T. A. Johnson, D. E. Dedrick, J. E. Miller, E. B. Stechel, C. T. Maravelias, Methanol production from CO_2 using solar-thermal energy: Process development and techno-economic analysis. *Energy Environ. Sci.* **4**, 3122–3132 (2011).
21. W. C. Chueh, C. Falter, M. Abbott, D. Scipio, P. Furler, S. M. Haile, A. Steinfield, High-flux solar-driven thermochemical dissociation of CO_2 and H_2O using nonstoichiometric ceria. *Science* **330**, 1791–1801 (2010).
22. J. A. Herron, J. Kim, A. A. Upadhye, G. W. Huber, C. T. Maravelias, A general framework for the assessment of solar fuel technologies. *Energy Environ. Sci.* **8**, 126–157 (2015).
23. F. Jiao, J. Li, X. Pan, J. Xiao, H. Li, H. Ma, M. Wei, Y. Pan, Z. Zhou, M. Li, S. Miao, J. Li, Y. Zhu, D. Xiao, T. He, J. Yang, F. Qi, Q. Fu, X. Bao, Selective conversion of syngas to light olefins. *Science* **351**, 1065–1068 (2016).
24. Q. Zhang, J. Kang, Y. Wang, Development of novel catalysts for Fischer–Tropsch synthesis: Tuning the product selectivity. *ChemCatChem* **2**, 1030–1058 (2010).
25. W. Sun, C. Qian, L. He, K. K. Ghuman, A. P. Y. Wong, J. Jia, A. A. Jelle, P. G. O'Brien, L. M. Reyes, T. E. Wood, A. S. Helmy, C. A. Mims, C. V. Singh, G. A. Ozin, Heterogeneous reduction of carbon dioxide by hydride-terminated silicon nanocrystals. *Nat. Commun.* **7**, 12553 (2016).
26. J. R. Scheffe, A. Steinfeld, Oxygen exchange materials for solar thermochemical splitting of H_2O and CO_2: A review. *Mater. Today* **17**, 341–348 (2014).
27. C. L. Muhich, B. D. Ehrhart, I. Al-Shankiti, B. J. Ward, C. B. Musgrave, A. W. Weimer, A review and perspective of efficient H_2 generation via solar thermal water splitting. *WIREs Energy Environ.* **5**, 261–287 (2016).
28. A. Demont, S. Abandes, E. Beche, Investigation of perovskite structures as oxygen-exchange redox materials for hydrogen production from thermochemical two-step water-splitting cycles. *J. Phys. Chem. C* **118**, 12682–12692 (2014).
29. A. H. McDaniel, E. C. Miller, D. Arifin, A. Ambrosini, E. N. Coker, R. Hyre, W. C. Chueh, J. Tong, Sr- and Mn-doped $LaAlO_{3-\delta}$ for solar thermochemical H_2 and CO production. *Energy Environ. Sci.* **6**, 2424–2428 (2013).
30. D. Arifin, V. J. Aston, X. H. Liang, A. H. McDaniel, A. W. Weimer, $CoFe_2O_4$ on a porous Al_2O_3 nanostructure for solar thermochemical CO_2 splitting. *Energy Environ. Sci.* **5**, 9438–9443 (2012).
31. P. Furler, J. Scheffe, M. Gorbar, L. Moes, U. Vogt, A. Steinfeld, Solar thermochemical CO_2 splitting utilization of reticulated porous ceria redo system. *Energy Fuels* **26**, 7051–7059 (2012).
32. A. Steinfeld, High-temperature solar thermochemistry for CO_2 mitigation in the extractive metallurgical industry. *Energy* **22**, 311–316 (1997).
33. L. C. Buelens, V. V. Galvita, H. Poelman, C. Detavernier, G. B. Marin, Super-dry reforming of methane intensifications CO_2 utilization via Le Chatelier's principle. *Science* **354**, 449–452 (2016).
34. V. V. Galvita, H. Poelman, C. Detavenier, G. B. Marin, Catalyst-assisted chemical looping for CO_2 conversion to CO. *Appl. Catal. B* **164**, 184–191 (2015).

35. V. V. Galvita, H. Poelman, V. Bliznuk, C. Detavenier, G. B. Marin, CeO_2-modified Fe_2O_3 for CO_2 utilization via chemical looping. *Ind. Chem. Eng. Res.* **52**, 8416–8426 (2013).
36. F. He, F. Li, Perovskite promoted iron oxide for hybrid water-splitting and syngas generation with exceptional conversion. *Energy Environ. Sci.* **8**, 535–539 (2015).
37. S. Bhavsar, M. Najera, G. Veser, Chemical looping dry reforming as novel, intensified process for CO_2 activation. *Chem. Eng. Technol.* **35**, 1281–1290 (2012).
38. M. Najera, R. Solunker, T. Gardner, G. Veser, Carbon capture and utilization via chemical looping dry reforming. *Chem. Eng. Res. Des.* **89**, 1533–1543 (2011).
39. L.-S. Fan, L. Zeng, S. Luo, Chemical looping technology platform. *AIChE J.* **61**, 2–22 (2015).
40. A. Fossdal, M.-A. Einarsrud, T. J. Grande, Phase equilibria in the pseudo-binary system $SrO–Fe_2O_3$. *J. Solid State Chem.* **117**, 2933–2942 (2004).
41. A. Demont, S. Abanades, Solar thermochemical conversion of CO_2 into fuel via two-step redox cycling of non-stoichiometric Mn-containing perovskite oxides. *J. Mater. Chem. A* **3**, 3536–3546 (2015).
42. A. H. Bork, M. Kubicek, M. Struzik, J. L. M. Rupp, Perovskite $La_{0.6}Sr_{0.4}Cr_{1-x}$ $Co_xO_{3-\delta}$ solid solutions for solar-thermochemical fuel production: Strategies to lower the operation temperature. *J. Mater. Chem. A* **3**, 15546–15557 (2015).
43. L. M. Neal, A. Shafiefarhood, F. Li, Dynamic methane partial oxidation using a Fe_2O_3@$La_{0.8}Sr_{0.2}FeO_{3-\delta}$ core–shell redox material in the absence of gaseous oxygen. *ACS Catal.* **4**, 3560–3569 (2014).
44. J.-F. Wu, S.-M. Yu, W.D. Wang, Y.-X. Fan, S. Bai, C.-W. Zhang, Q. Gao, J. Huang, W. Wang, Mechanistic insight into the formation of acetic acid from the direct conversion of methane and carbon dioxide on zinc-modified H–ZSM-5 zeolite. *J. Am. Chem. Soc.* **135**, 13567–13573 (2013).
45. W. L. Luyben, Design and control of a methanol reactor/column process. *Ind. Eng. Chem. Res.* **49**, 6150–6163 (2010).
46. J. H. Jones, The Cativa™ process for the manufacture of acetic acid. *Platinum Metals Rev.* **44**, 94–105 (2000).
47. U.S. National Energy Technology Laboratory, Types of coal-derived chemicals (U.S. Department of Energy, 2016); www.netl.doe.gov/research/coal/energy-systems/gasification/gasifipedia/coal-derived-chem [accessed 18 June 2017].
48. K. C. Waugh, Methanol synthesis. *Catal. Lett.* **142**, 1153–1166 (2012).
49. L. R. Merte, G. Peng, R. Bechstein, F. Rieboldt, C. A. Farberow, L. C. Grabow, W. Kudernatsch, S. Wendt, E. Lægsgaard, M. Mavrikakis, F. Besenbacher, Water-mediated proton hopping on an iron oxide surface. *Science* **336**, 889–893 (2012).
50. L. S. Fan, *Chemical Looping System for Fossil Energy Conversion* (John Wiley & Sons, 2011).
51. G. T. Rochelle, Amine scrubbing for CO_2 capture. *Science* **325**, 1652–1654 (2009).
52. F. He, F. Li, Hydrogen production from methane and solar energy-process evaluations and comparison studies. *Int. J. Hydrogen Energy* **39**, 18092–18102 (2014).

Acknowledgments: We thank A. Shafiefarhood and Y. Liu for collecting the TEM images, Y. Gao for acquiring the SEM micrographs, N. Galinsky for collecting the in situ XRD patterns, and T. Y. Li for the Rietveld analysis of XRD patterns at the North Carolina (NC) State University. **Funding:** This work was supported by the NSF (CBET-1254351 and CBET-1510900) and the Kenan Institute at NC State University. **Author contributions:** F.L. conceived and supervised the study. J.Z. and F.L. designed the study and wrote the manuscript. J.Z. carried out the experiments and analyzed the data. V.H. carried out the ASPEN Plus simulation and collected the XRD data. **Competing interests:** The authors declare that they have no competing interests. **Data and materials availability:** All data needed to evaluate the conclusions in the paper are present in the paper and/or the Supplementary Materials. Additional data related to this paper may be requested from the authors.

Submitted 13 April 2017
Accepted 3 August 2017
Published 30 August 2017
10.1126/sciadv.1701184

Citation: J. Zhang, V. Haribal, F. Li, Perovskite nanocomposites as effective CO_2-splitting agents in a cyclic redox scheme. *Sci. Adv.* **3**, e1701184 (2017).

Perovskite nanocomposites as effective CO_2-splitting agents in a cyclic redox scheme

Junshe Zhang, Vasudev Haribal and Fanxing Li

Sci Adv **3** (8), e1701184.
DOI: 10.1126/sciadv.1701184